

Electronic Supporting Information

Partially fluorinated MIL-101(Cr): from a minuscule structure modification to a huge chemical environment transformation inspected by ^{129}Xe NMR

Mariana L. Díaz-Ramírez,^{†a} Elí Sánchez-González,^{†a} J. Raziel Álvarez,^a Gerardo A. González-Martínez,^a Satoshi Horike,^b Kentaro Kadota,^b Kenji Sumida,^c Eduardo González-Zamora,^d Marie-Anne Springuel-Huet,^e Aída Gutiérrez-Alejandro,^f Vojtech Jancik,^g Shuhei Furukawa,^{*,b} Susumu Kitagawa,^b Illich A. Ibarra^{*,a} and Enrique Lima^{*,a}

^a*Laboratorio de Fisicoquímica y Reactividad de Superficies (LaFReS), Instituto de Investigaciones en Materiales, Universidad Nacional Autónoma de México, Circuito Exterior s/n, CU, Del. Coyoacán, 04510, Ciudad de México, Mexico.*

^b*Institute for Integrated Cell-Material Sciences (iCeMS), Kyoto University, 606-8501 Kyoto, Japan.*

^c*Departamento de Química, Universidad Autónoma Metropolitana-Iztapalapa, San Rafael Atlixco 186, Col. Vicentina, Iztapalapa, C. P. 09340, Ciudad de México, Mexico.*

^d*Centre for Advanced Nanomaterials, School of Physical Sciences, The University of Adelaide, South Australia 5005, Australia.*

^e*UMR7574 Chimie de la Matière Condensée de Paris (LCMCP), Paris, France.*

^f*UNICAT, Departamento de Ingeniería Química, Facultad de Química, Universidad Nacional Autónoma de México (UNAM), Coyoacán, Ciudad de México, Mexico.*

^g*Centro Conjunto de Investigación en Química Sustentable UAEM-UNAM, Carr. Toluca-Atlacomulco Km 14.5, Toluca, Estado de México 50200, México. Personal del Instituto de Química de la UNAM.*

Table of contents

S1.	Details for the generation of Figure 1.....	3
S2.	Thermogravimetric analysis	3
S3.	Bulk powder XRD.....	4
S4.	N ₂ adsorption isotherms.....	5
S5.	Solids recovered from mother liquor and washings of MIL-101(Cr)-4F(1%).....	7
S6.	Elemental analysis	7
S7.	Isosteric heat of adsorption of H ₂ O, CO ₂ , O ₂ and H ₂	8
S8.	CO ₂ Diffusion Coefficient.....	13
S9.	CO ₂ /N ₂ Selectivity.....	15
S10.	O ₂ capture	16
S11.	¹²⁹ Xe spectra	17
S12.	I ₂ desorption	19
S13.	H ₂ S adsorption experiments	21

S1. Details for the generation of Figure 1

Prior to the substitution, the geometry of the different crystallographically independent BDC molecules was adjusted so that the phenylene rings were planar and coplanar with the carbon atoms of the carboxylate groups. Also, the geometry of the carboxylate groups was restrained to be coplanar with the adjacent carbon atom of the phenylene ring. Thereafter, the hydrogen atoms were replaced by fluorine with a C-F distance of 1.345 Å (mean C_{Ar}-F bond length obtained from the CSD database). These two models were used to visualise the voids present in the networks and calculate their volume using probe radius of 1.2 Å and Grid spacing of 0.7 Å within the Mercury program.[1]

S2. Thermogravimetric analysis

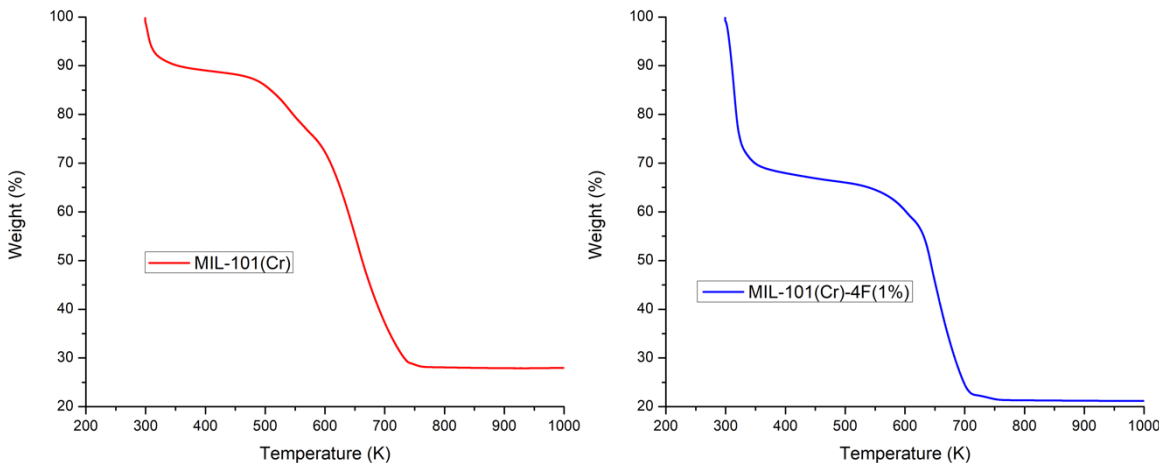


Fig. S1. TGA of: (left) as-synthesised MIL-101(Cr) and (right) and as-synthesised MIL-101(Cr)-4F(1%).

S3. Bulk powder XRD

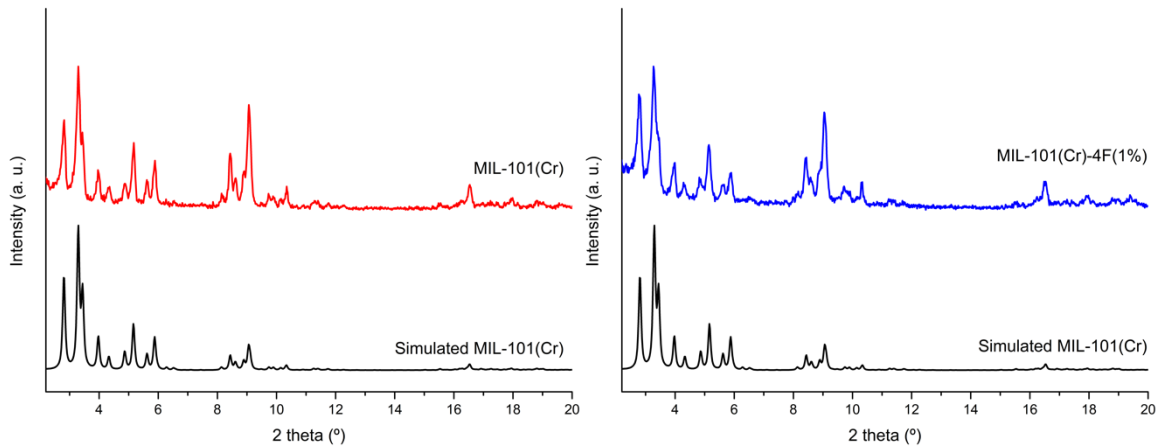


Fig. S2. PXRD patterns of: (left) simulated and MIL-101(Cr) (black), as-synthesised MIL-101(Cr) (red); and (right) simulated MIL-101(Cr) (black) and as-synthesised MIL-101(Cr)-4F(1%) (blue).

S4. N₂ adsorption isotherms

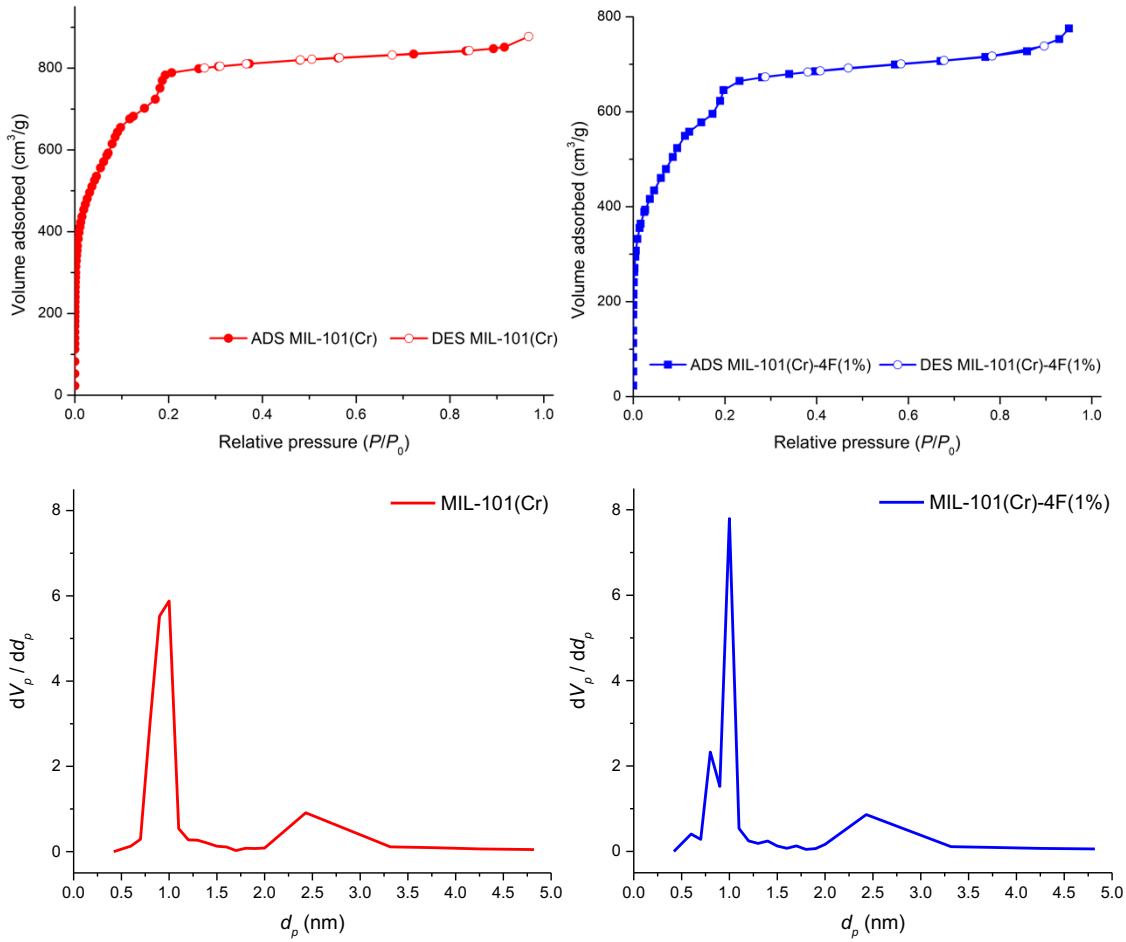


Fig. S3. Nitrogen adsorption-desorption isotherms of: (left) as-synthesised MIL-101(Cr) and (right) as-synthesised MIL-101(Cr)-4F(1%). Pore size distribution of each sample (bottom).

Another fluorinated sample was synthesised, MIL-101(Cr)-4F(2%) (Elemental analysis; calculated: C=41.19, H=1.62, F=2.00; found: C=41.23, H=1.57, F=2.05 (Fig. S4), which exhibited less crystallinity, reduced BET surface area ($1310 \text{ m}^2 \text{ g}^{-1}$) and CO_2 uptake .

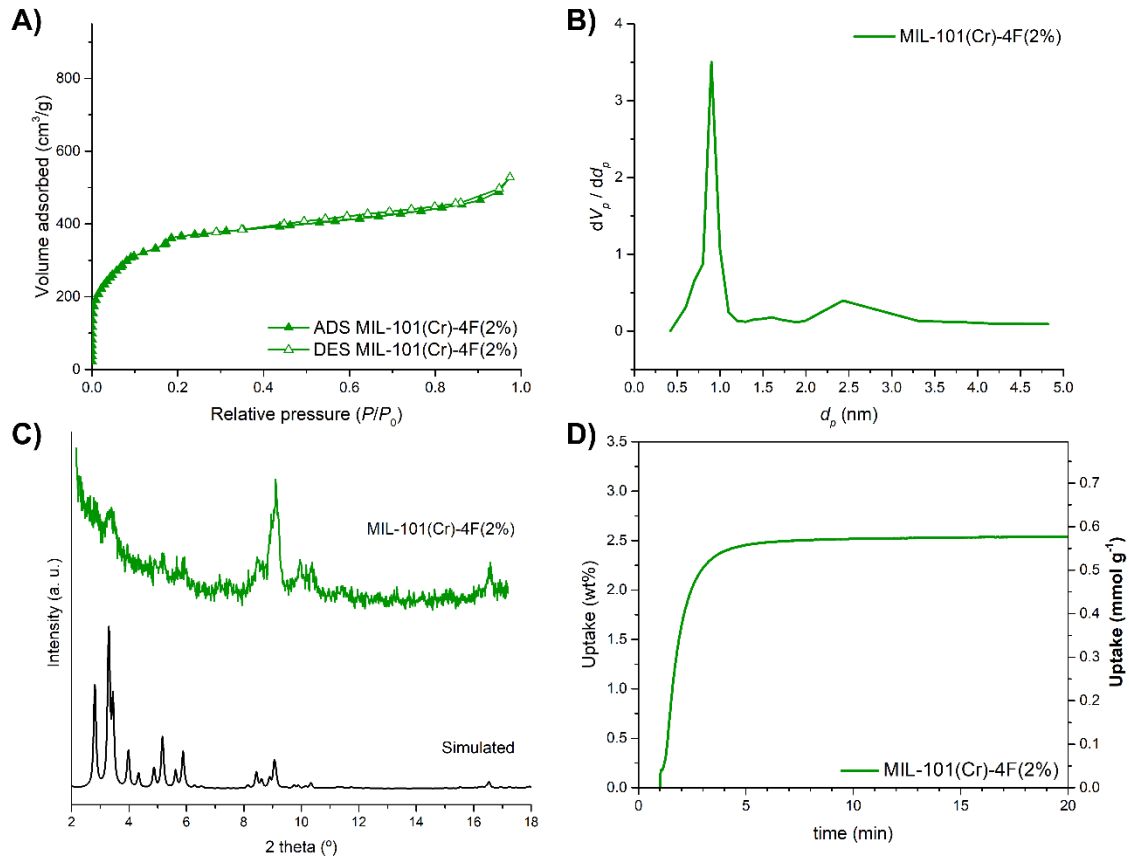


Fig. S4. MIL-101(Cr)-4F(2%). Nitrogen adsorption-desorption isotherm at 77 K A), pore size distribution of each sample B), PXRD pattern C), and kinetic CO_2 uptake at 303 K D).

S5. Solids recovered from mother liquor and washings of MIL-101(Cr)-4F(1%)

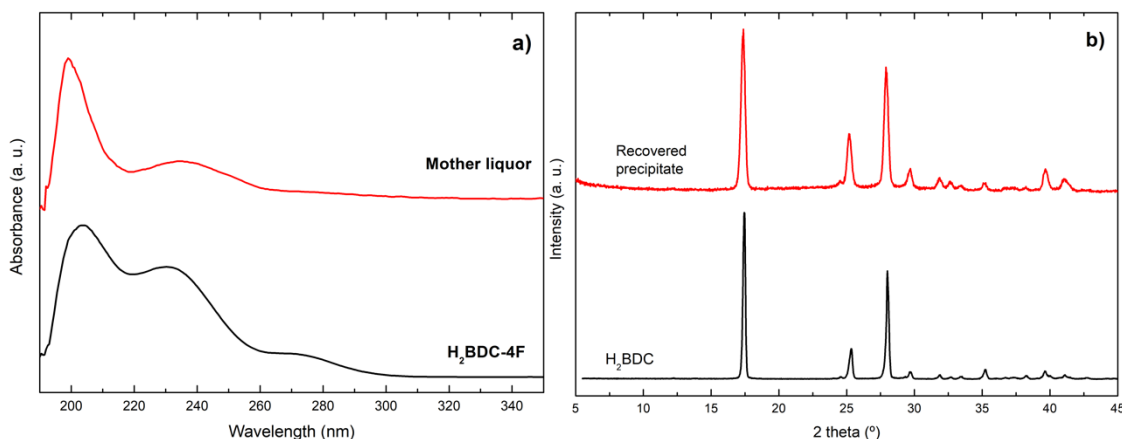


Fig. S5 a) UV/vis spectrum of the mother liquor retrieved after synthesis (red) compared to the spectrum of H₂BDC-4F (black) and b) PXRD patterns of H₂BDC-4F (black) and recovered precipitate after washings with diluted NaOH (red).

S6. Elemental analysis

Table S1. Elemental analysis data for MIL-101(Cr)-4F(1%) as-synthesised sample, [Cr₃O(BDC)_{3-x}(BDC-F₄)_x]·Cl(H₂O)_m(DMF)_n.

Element	Calculated	Run					Average
		1	2	3	4	5	
C	34.18	34.63	33.92	34.61	32.52	35.58	34.25
H	4.37	4.32	4.23	4.42	3.98	4.52	4.29
N	2.21	2.32	2.27	2.09	2.25	2.31	2.25
F	0.65	0.67	0.59	0.67	0.58	0.68	0.64

Table S2. Elemental analysis data for MIL-101(Cr)-4F(1%) activated sample, [Cr₃O(BDC)_{3-x}(BDC-F₄)_x]·Cl.

Element	Calculated	Run					Average
		1	2	3	4	5	
C	34.18	40.23	42.48	42.38	40.73	39.58	41.08
H	4.37	1.81	1.91	1.86	1.79	1.73	1.82
F	0.65	0.93	0.98	0.95	0.912	0.87	0.93

S7. Isosteric heat of adsorption of H₂O, CO₂, O₂ and H₂

The heat of adsorption of H₂O, CO₂, O₂ and H₂, ΔH , was calculated by the isosteric method for the MIL-101(Cr) and MIL-101(Cr)-4F(1%), using the corresponding adsorption isotherms at two different temperatures (Fig. S5-8A and Fig. S5-8B). A virial-type equation was used to fit the adsorption isotherms:

$$\ln\left(\frac{n}{p}\right) = A_0 + A_1 n + A_2 n^2 + \dots \quad \text{Eq. S5.1}$$

where p is the pressure, n is the amount adsorbed and A_0, A_1, \dots are the virial coefficients (A_2 and higher terms can be ignored at lower coverage values). A plot of $\ln(n/p)$ versus n should give a straight line at low surface coverage (Fig. S5-8C and Fig. S5-8D).

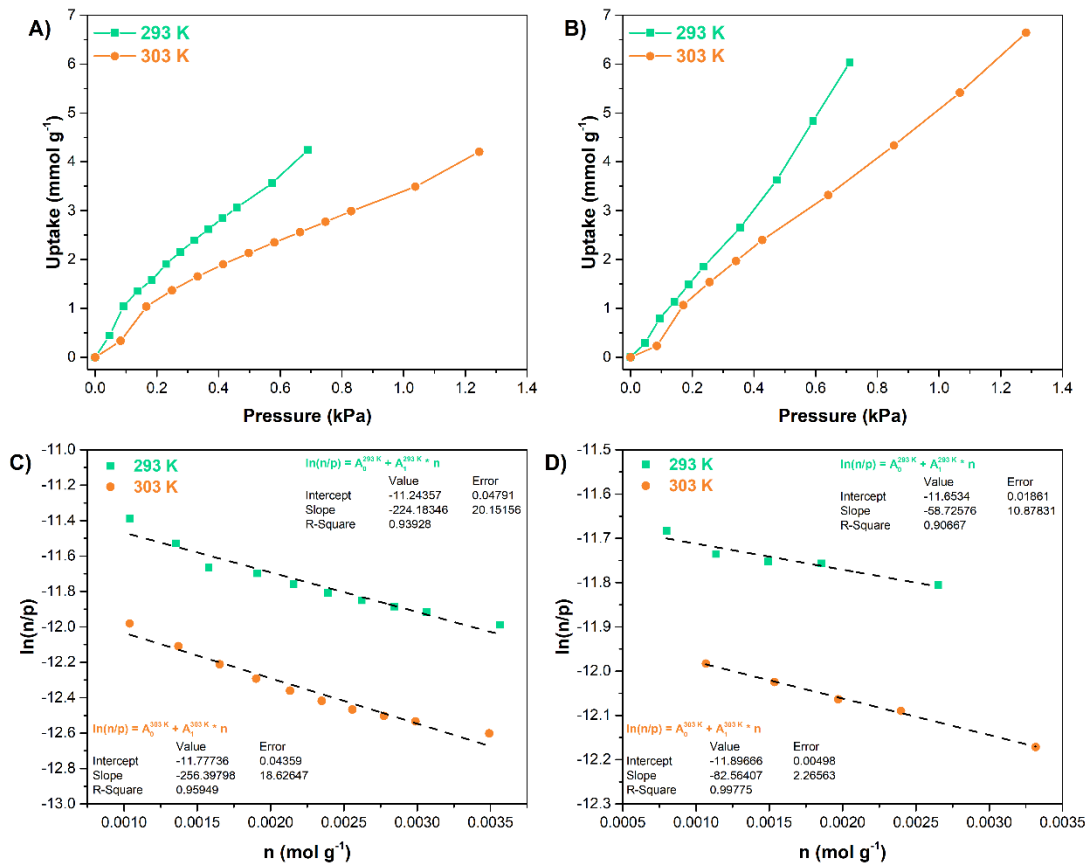


Fig. S6. Water adsorption isotherms at 293 and 303 K for A) MIL-101(Cr) and B) MIL-101(Cr)-4F(1%) virial fitting plots for C) MIL-101(Cr) and D) MIL-101(Cr)-4F(1%) at 293 and 303 K.

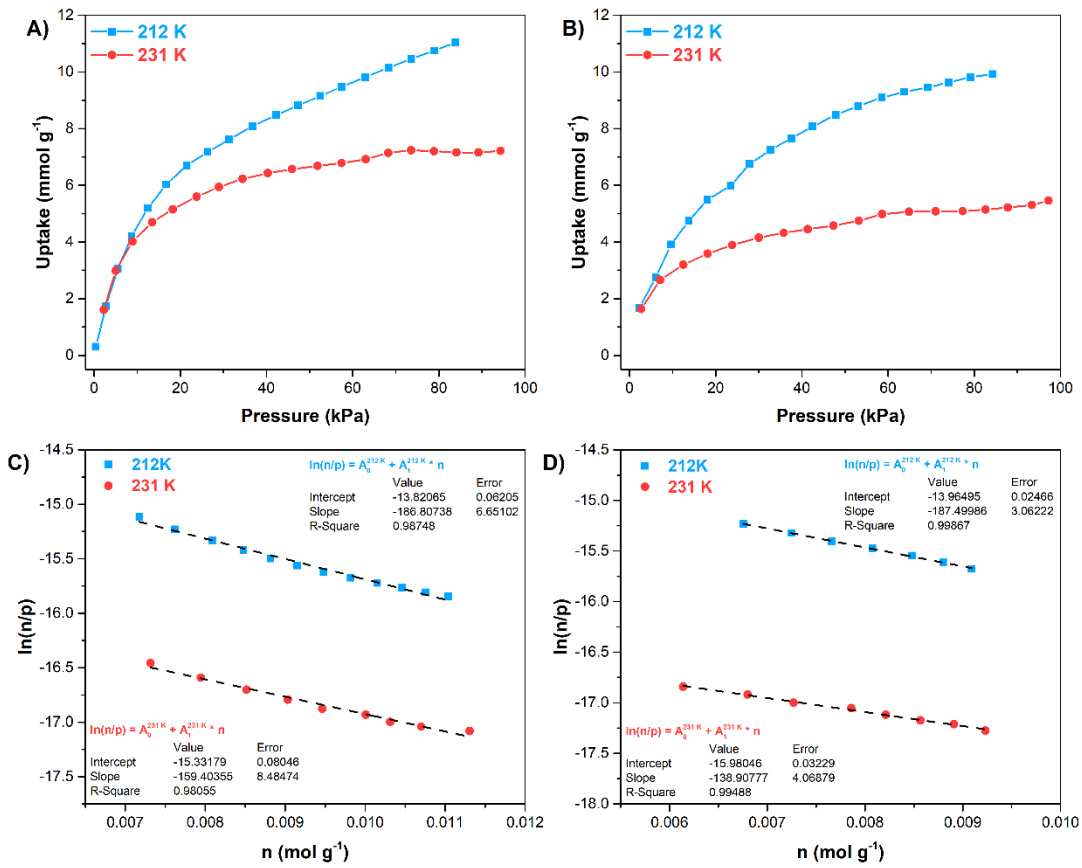


Fig. S7. CO₂ adsorption isotherms at 212 and 231 K for A) MIL-101(Cr) and B) MIL-101(Cr)-4F(1%); virial fitting plots for C) MIL-101(Cr) and D) MIL-101(Cr)-4F(1%) at 212 and 231 K.

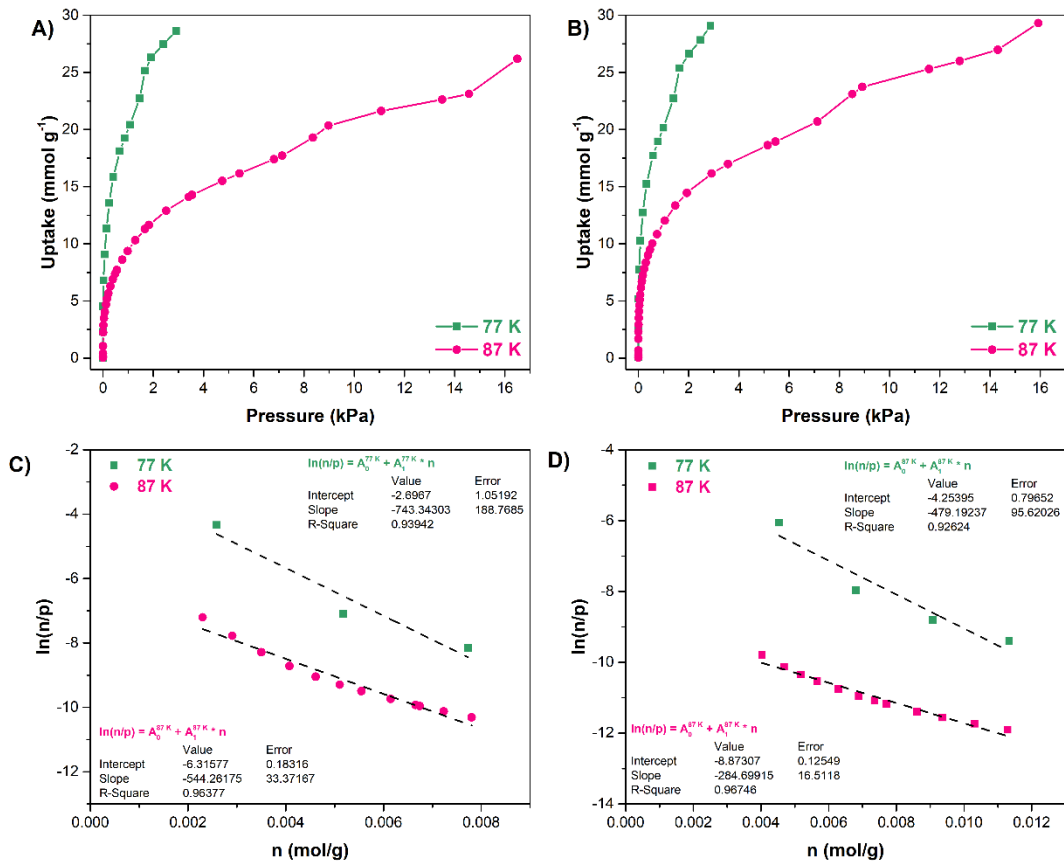


Fig. S8. O₂ adsorption isotherms at 77 and 87 K for A) MIL-101(Cr) and B) MIL-101(Cr)-4F(1%) virial fitting plots for C) MIL-101(Cr) and D) MIL-101(Cr)-4F(1%) at 77 and 87 K.

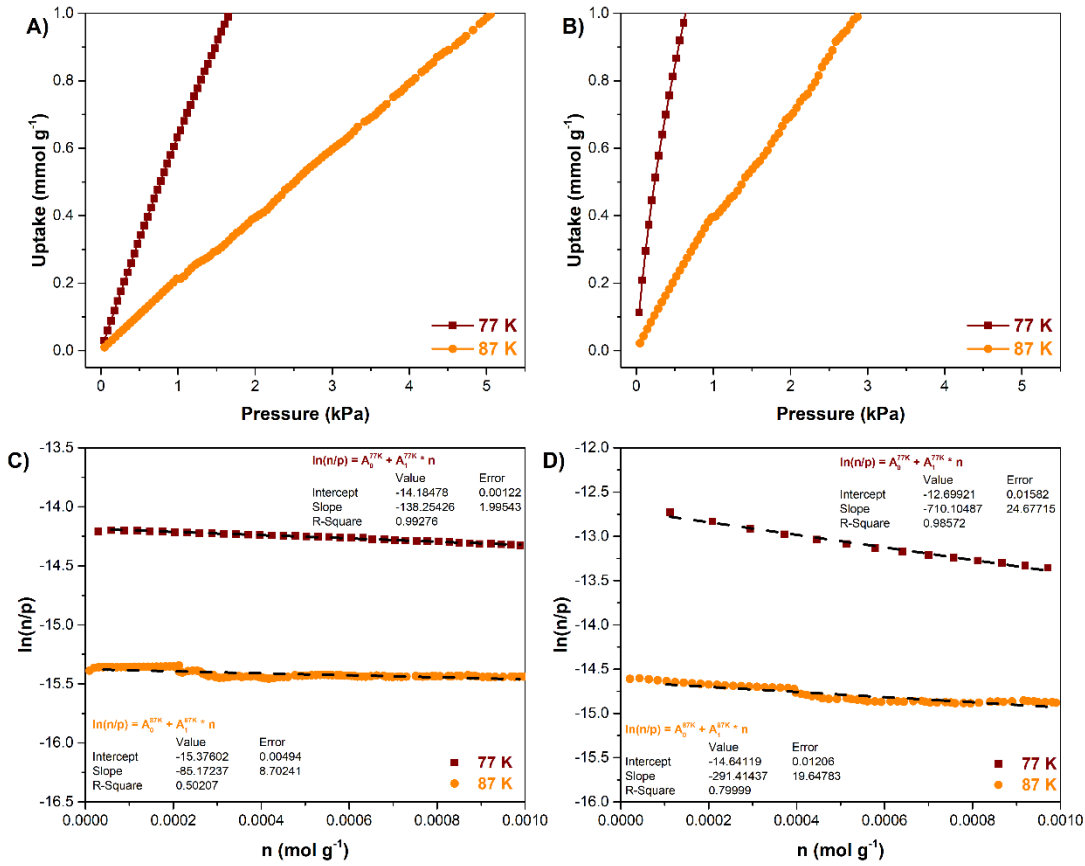


Fig. S9. H₂ adsorption isotherms at 77 and 87 K for A) MIL-101(Cr) and B) MIL-101(Cr)-4F(1%) virial fitting plots for C) MIL-101(Cr) and D) MIL-101(Cr)-4F(1%) at 77 and 87 K.

Using the Clausius Clapeyron equation (Eq. S5.2) for a fixed surface coverage (θ), the Eq. S5.3 is obtained. By the substitution of p in Eq. S5.3 with Eq. S5.1, results an expression of the isosteric heat of adsorption (Eq. S5.4). From the linear fittings, the virial coefficients are used to estimate the isosteric heat of adsorption (Table S).

$$\left(\frac{\partial \ln(p)}{\partial T}\right)_\theta = \frac{Q_{ST}}{RT^2} \quad \text{Eq. S5.2}$$

$$\ln\left(\frac{p_1}{p_2}\right) = \frac{Q_{ST}}{R} \left(\frac{1}{T_2} - \frac{1}{T_1}\right) \quad \text{Eq. S5.3}$$

$$Q_{ST} = R[(A_0^{T_2} - A_0^{T_1}) + (A_1^{T_2} - A_1^{T_1})n] \left(\frac{T_1 T_2}{T_1 - T_2}\right) \quad \text{Eq. S5.4}$$

Table S3. Isosteric Heat of Adsorption values at zero loading of CO₂, O₂, H₂ and H₂O for MIL-101(Cr) and MIL-101(Cr)-4F(1%).

Material	<i>Q_{ST}</i> (kJ mol ⁻¹)			
	CO ₂	O ₂	H ₂	H ₂ O
MIL-101(Cr)	32.4	20.3	6.6	39.7
MIL-101(Cr)-4F(1%)	43.2	25.7	10.8	18.2

Additionally, from the estimation of the enthalpy at zero loading we calculated the enthalpy of adsorption at different loadings (θ) using Eq. S5.3 (Fig. S9).

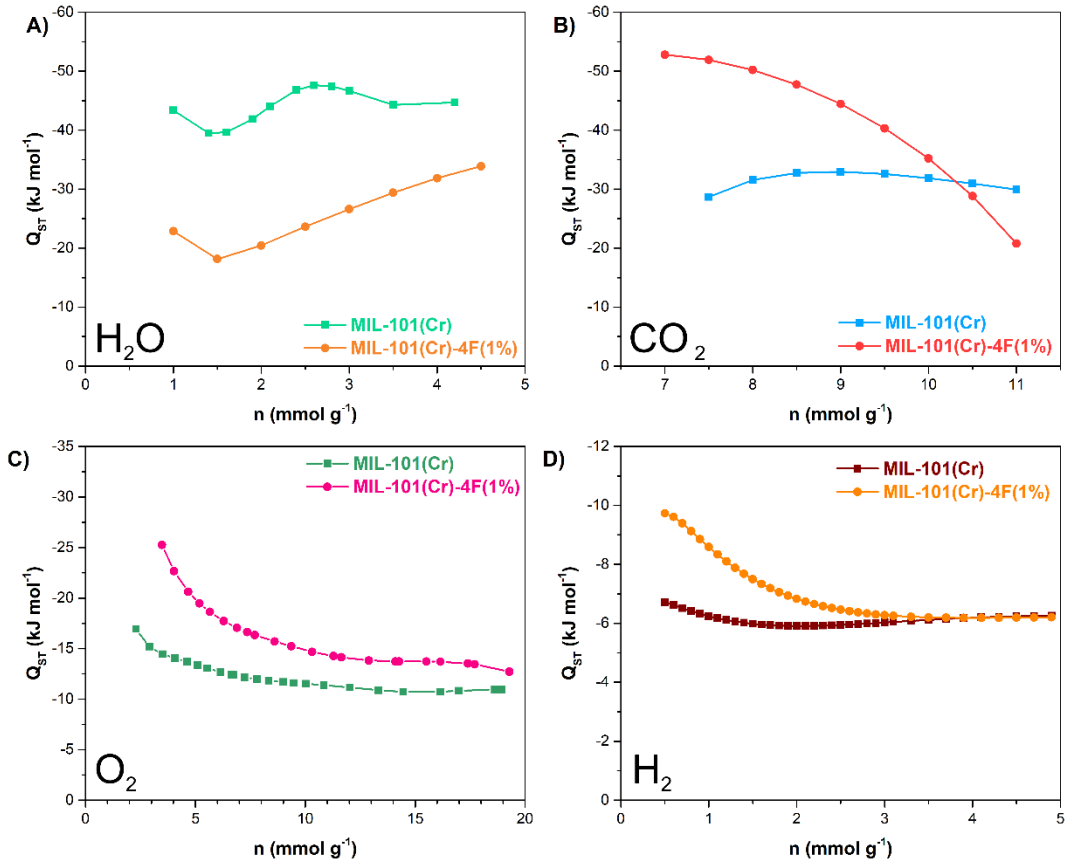


Fig. S10. Isosteric heat of adsorption (Q_{ST}) at different loadings of A) H₂O, B) CO₂, C) O₂ and D) H₂ for the MIL-101(Cr) and MIL-101(Cr)-4F(1%) samples

S8. CO₂ Diffusion Coefficient

Adsorption isotherms at 303 K of MIL-101(Cr) and MIL-101(Cr)-4F(1%) were measured.

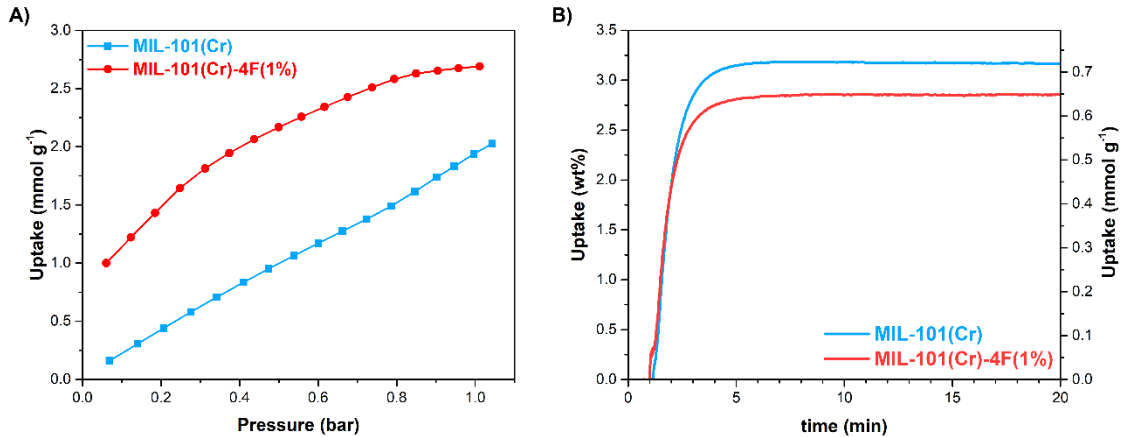


Fig. S11. CO₂ adsorption isotherms at 303 K A) and kinetic uptake experiments at 303 K B), for the MIL-101(Cr) and MIL-101(Cr)-4F(1%) samples.

Diffusion time constants (D_M/r_c^2) were estimated from the kinetic uptake experiments. The original set of data was normalized to fractional uptake, the ratio of the uptake (q_t) to the equilibrium uptake (q_e). Assuming diffusion into porous spheres the Eq. S6.1 describes the relationship between the fractional transient uptake and time.[2]

$$\frac{q_t}{q_e} \cong \frac{6}{r_c} \sqrt{\frac{D_M t}{\pi}} \quad \text{Eq. S6.1}$$

We plotted the fractional transient uptake (q_t/q_e) versus the square root of time ($t^{1/2}$) (Fig. S9). A linear fit can be obtained from the lower adsorption data (0.1-0.6 q_t/q_e), where the slope is represented by Eq. S6.2. Rearranging the Eq. S6.2 we obtain the Eq. S6.3 from which the diffusion time constant (D_M/r_c^2) was estimated. Intercrystallite diffusivity (D_M) was estimated in all cases using the same crystallite radius (r_c), 0.145 and 0.043 μm for MIL-101(Cr) and MIL-101(Cr)-4F(1%) respectively (Fig. S10).

$$m = \frac{6}{r_c} \sqrt{\frac{D_M}{\pi}} \quad \text{Eq. S6.2}$$

$$\frac{D_M}{r_c^2} = \frac{\pi m^2}{36} \quad \text{Eq. S6.3}$$

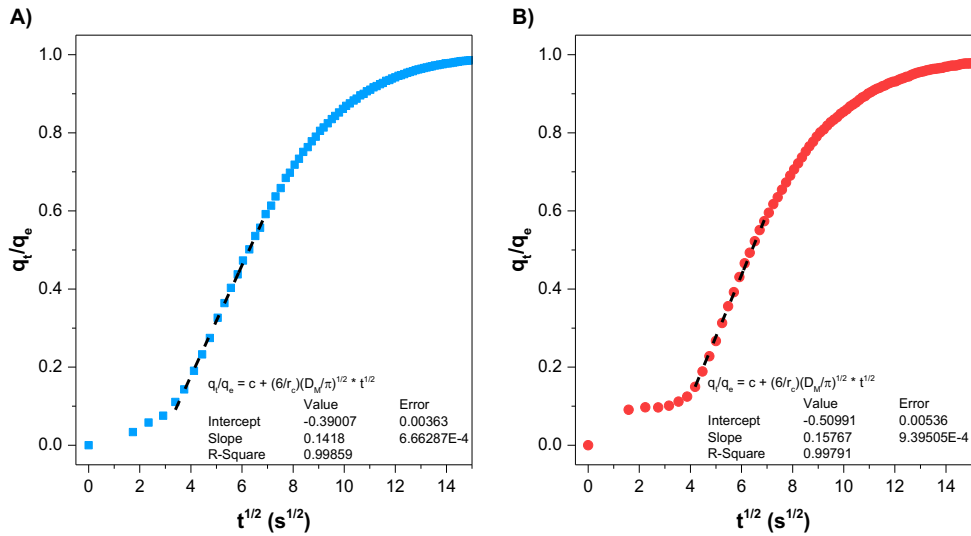


Fig. S12. CO₂ fractional transient uptake versus the square root of time at 303K for A) MIL-101(Cr) and B) MIL-101(Cr)-4F(1%).

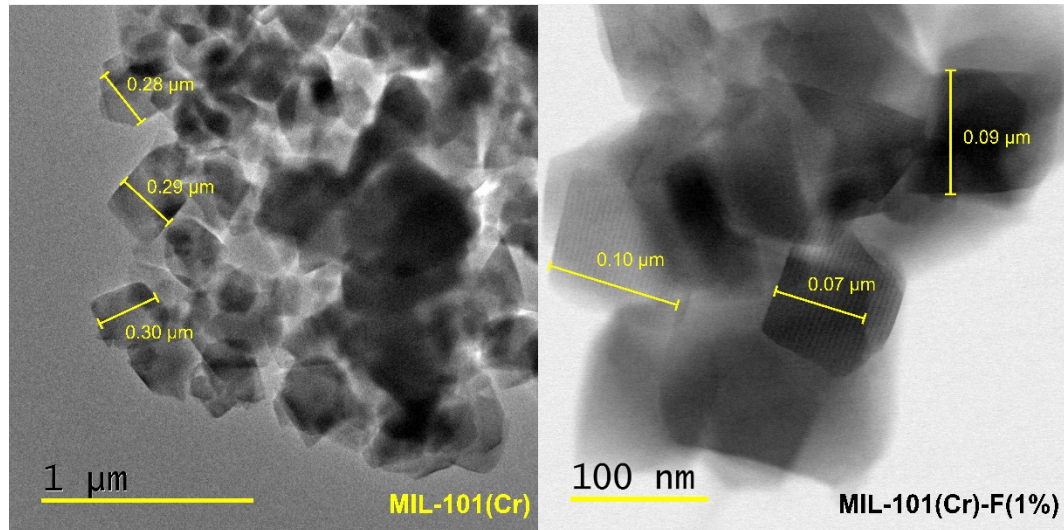


Fig. S13. TEM micrographs for MIL-101(Cr) (left) and MIL-101(Cr)-4F(1%) (right).

Table S4. CO₂ Diffusion data for MIL-101(Cr) and MIL-101(Cr)-4F(1%).

Material	$D_M/r_c^2 (10^{-3} \text{ s}^{-1})$	$r_c (\mu\text{m})$	$D_M (10^{-12} \text{ cm}^2 \text{ s}^{-1})$
MIL-101(Cr)	1.75	0.145	36.7
MIL-101(Cr)-4F(1%)	2.17	0.043	4.0

S9. CO₂/N₂ Selectivity

Adsorption isotherms at 313 K were measured to assess the CO₂/N₂ selectivity of MIL-101(Cr) and MIL-101(Cr)-4F(1%) (Fig. S11). A typical post-combustion flue gas composition contains a 75% of N₂, 15% of CO₂ and the rest of other gases. The selectivity factor (*S*) is defined as the molar ratio of the adsorption quantities (*q_i*) normalized at the corresponding partial pressures of the gases (*p_i*) in a defined mixture (Eq. S7.1). In the case of post-combustion CO₂ capture, these partial pressures are 0.15 and 0.75 bar for CO₂ and N₂ respectively.[3]

$$S = \frac{q_1/q_2}{p_1/p_2} \quad \text{Eq. S7.1}$$

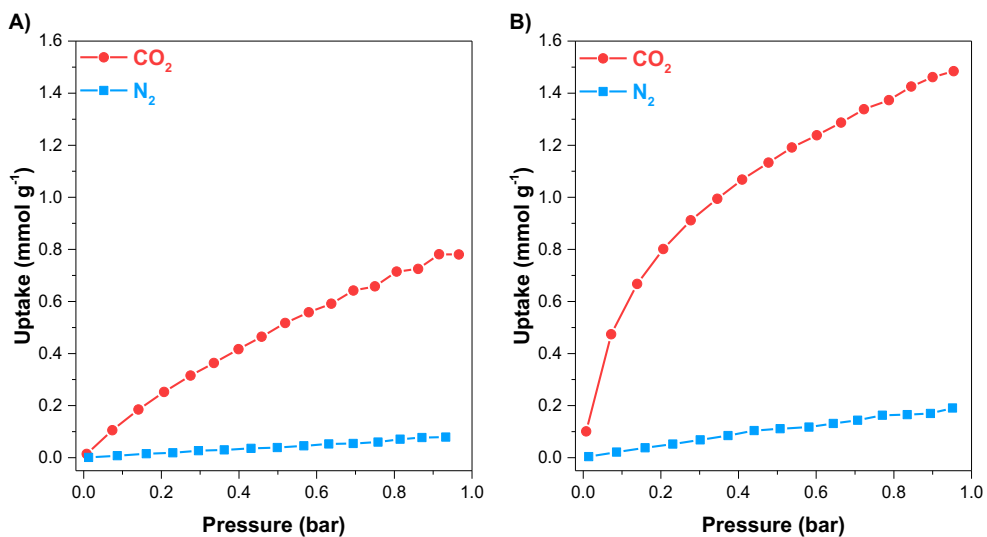


Fig. S14. CO₂ and N₂ adsorption isotherms at 313 K for A) MIL-101(Cr) and B) MIL-101(Cr)-4F(1%).

Table S5. CO₂ and N₂ Uptake in MIL-101(Cr) and MIL-101(Cr)-4F(1%).

Material	CO ₂ uptake at 0.15 bar (mmol g ⁻¹)	N ₂ uptake at 0.75 bar (mmol g ⁻¹)	selectivity
MIL-101(Cr)	0.194	0.059	16.4
MIL-101(Cr)-4F(1%)	0.694	0.157	22.1

S10. O₂ capture

Oxygen storage is an uncommon MOF application, despite the high surface areas the tuning of oxygen adsorption has made this application cumbersome. Reducing the high pressures for oxygen storage can translate in safer and cheaper storage, this can be addressed by augmenting the oxygen adsorption in a porous matrix.[4-6] DeCoste, LeVan, Farha and co-workers, after a thorough computational screening, proved NU-125 as a benchmark porous material.[4] This material exhibited a 15.7 mmol g⁻¹ deliverable O₂ capacity at 298 K, nearly double as the amount an empty cylinder of oxygen at 140 bar.[4] Later, using a rational molecular building blocks approach, Eddaoudi and co-workers synthesised an aluminum based MOF with soc topology with exceptional adsorption properties.[5] Al-soc-MOF-1 showed the highest O₂ gravimetric capacity for a MOF, 27.5 mmol g⁻¹.[5] More recently, Moghada, Farha, Fairen-Jimenez and co-workers, reported another computational study where volumetric capacity was the target, they found in UMCM-152 the highest O₂ storage capacity (249 cm³(STP) cm⁻³).[6] All his materials present great surface areas (Table S4), but tuning the pore may be an alternative to increase their oxygen capacity. Piscopo and co-workers, studied the impact of UiO-66 with fluorinated ligands in the oxygen adsorption.[7] They reported a 1.3-fold increment in the O₂ uptake at 298 K, a modest capture of 3.1 mmol g⁻¹ at 90 bar.[7]

Following this example, MIL-101(Cr)-4F(1%) a fluorinated-mesoporous material was evaluated for oxygen storage. The MIL-101(Cr)-4F(1%) O₂ adsorption isotherm at 298 K presents a significant enhancement compared with the original material (Fig.S11), at 90 bar registered an uptake of 13 mmol g⁻¹ 2.5-fold more than the MIL-101(Cr). Using the Toth model, the adsorption at 140 bar was estimated and the deliverable amount of O₂ calculated. The MIL-101(Cr)-4F(1%) presented a 16.5 mmol g⁻¹ working capacity for O₂ storage, a significant improvement from the 5.3 mmol g⁻¹ obtained for the MIL-101(Cr) (Table S4). This 3.1-fold enhancement represents the small effect of the pore tuning with the fluorinated ligand, a reduction in the pore diameter and increase in the heat of adsorption.[8]

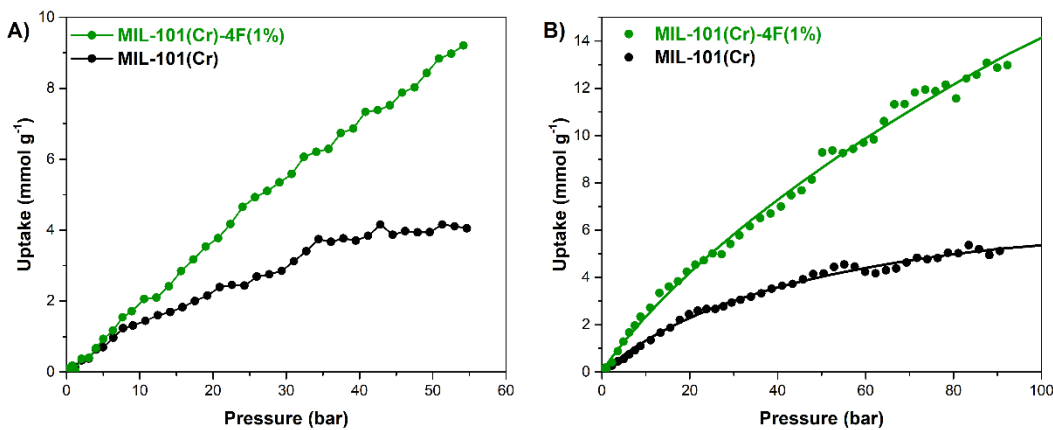


Fig. S15. Oxygen uptake at 298 K for MIL-101(Cr) and MIL-101(Cr)-4F(1%), adsorption at A) 55 bar and B) 90 bar. Circles represent experimental data and continuous lines represent Toth model fits.

Table S6. Surface area, pore volume, oxygen uptake capacities at selected pressures, and deliverable oxygen capacity of MIL-101(Cr), MIL-101(Cr)-4F(1%) and some relevant MOFs.

Material	BET surface area ($\text{m}^2 \text{ g}^{-1}$)	Pore Volume ($\text{cm}^3 \text{ g}^{-1}$)	Adsorbed O ₂ (mmol g ⁻¹)				Deliverable O ₂ ^a (mmol g ⁻¹)	REF.
			30 bar	50 bar	90 bar	140 bar		
Al-soc-MOF-1	5585	2.3	-	13.2	-	29	27.5	[5]
UMCM-152	3760	-	-	-	-	-	19.6	[6]
MIL-101(Cr)-4F(1%)	2176	1.19	5.4	8.6	13	17.8 ^b	16.5	This work
NU-125	2880	1.29	8.3	-	-	17.4	15.7	[4]
HKUST-1	1880	0.77	6.0	-	-	13.2	11.9	[4]
MIL-101(Cr)	2916	1.32	2.9	4	5.1	6.0 ^b	5.3	This work
UiO-66-CF3 25	1345	0.53	1.8	-	3.1	-	-	[7]
UiO-66	1571	0.60	1.7	2.1	2.3	-	-	[4]
UiO-66-F 25	1152	0.45	1.5	-	-	-	-	[4]

^a Uptake at 140 bar minus uptake at 5 bar,[4] ^b Estimated values using the Toth model.

S11. ¹²⁹Xe spectra

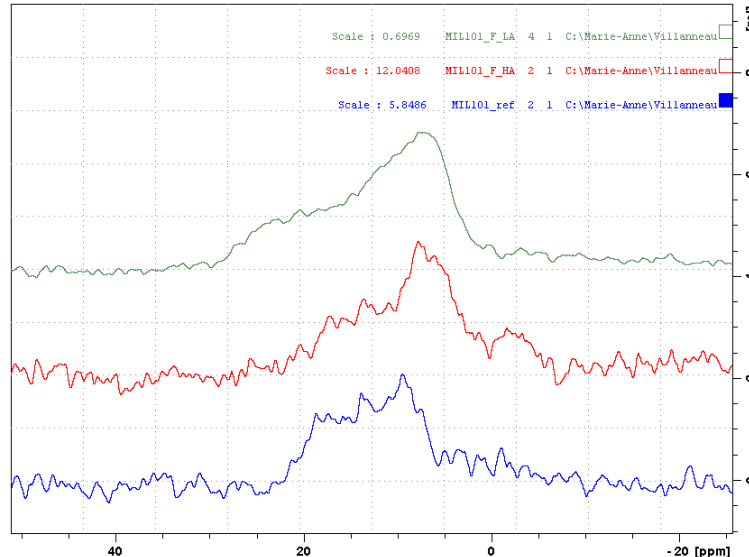


Fig. S16. Gas signal for P(Xe)= 750- 780 Torr.

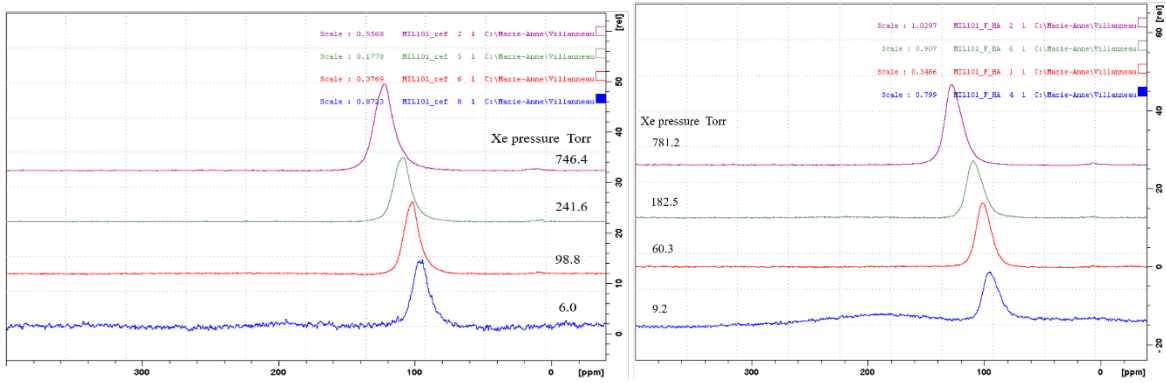


Fig. S17. Spectra of adsorbed ^{129}Xe at different loadings of: (left) MIL-101(Cr) and (right) MIL-101(Cr)-4F(1%).

S12. I₂ desorption

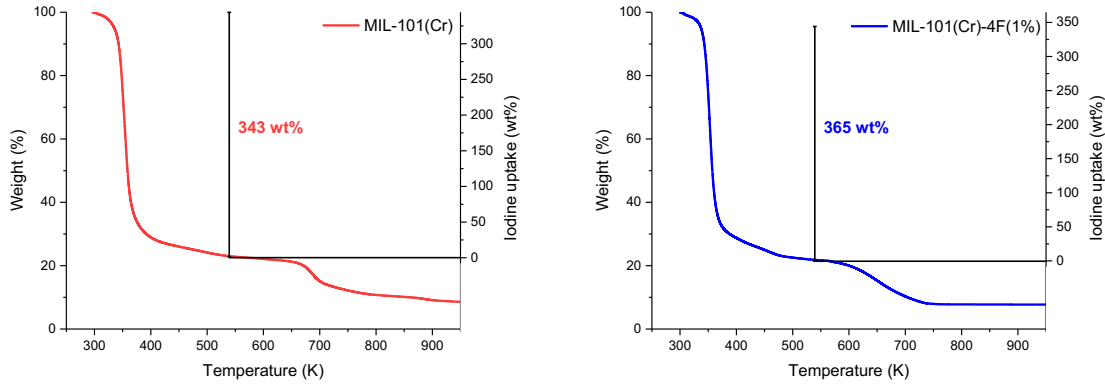


Fig. S18. TGA trace of the I₂ saturated samples: (left) MIL-101(Cr) and (right) MIL-101(Cr)-4F(1%), indicating the I₂ uptake.

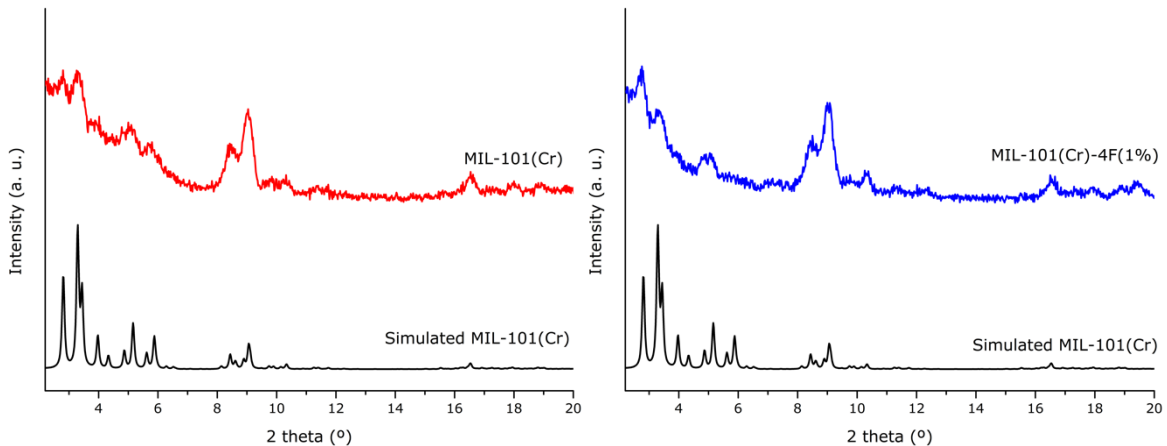


Fig. S19. PXRD of materials after being thermally treated to desorb I₂. (Left) simulated and MIL-101(Cr) (black), MIL-101(Cr) (red); and (right) simulated MIL-101(Cr) (black) and MIL-101(Cr)-4F(1%) (blue).

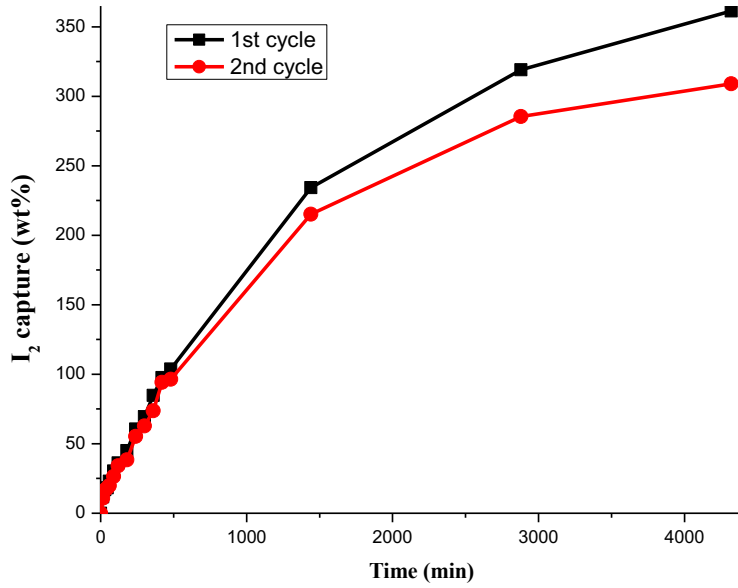


Fig. S20. Two cycles of kinetic I₂ uptake of MIL-101(Cr)-4F(1%) performed at 303 K.

Table S7. Iodine adsorption properties of selected porous materials.

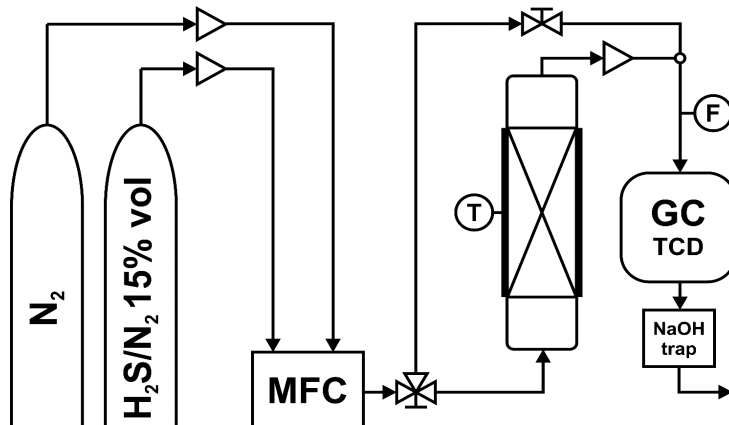
Material	Conditions	Temperature (K)	I ₂ uptake (wt%)	Ref.
MIL-101(Cr)-4F(1%)	Vapor	RT ^a	365	This work
HCMP-3	Vapor	358	316	[9]
HCMP-2	Vapor	358	281	[9]
Zr _x O _y (OH) _z (peb) _w	Vapor	RT	279	[10]
PAF-24	Vapor	343	276	[11]
PAF-23	Vapor	343	271	[11]
MIL-101(Cr)	Vapor	RT	343	This work
PAF-25	Vapor	343	260	[11]
[Zn _x (tptc)(apy) _{2-x} (H ₂ O) _w	Vapor	348	216	[12]
CMP-E1	Vapor	343	215	[11]
CMPN-3	Vapor	343	208	[13]
HKUST-1	Vapor	348	175	[14]
MIL-101(Cr)-TED	Vapor	303	174 ^b	[15]
(ZnI _x) _y (TPT) _z	Vapor	RT	173	[16]
MIL-101(Cr)-HMTA	Vapor	303	160 ^b	[15]
MFM-300(Sc)	Vapor	353	154	[17]
MFM-300(Fe)	Vapor	353	129	[17]
ZIF-8	Vapor	350	125	[18]
UiO-66-PYDC	Solution	RT	125	[19]
MFM-300(In)	Vapor	353	116	[17]
Ni _x (44pba) _y	Vapor	RT	110	[20]
Zr _x O _y (OH) _z (sdc) _w	Vapor	RT	107	[10]
Zn _x (DL-lac) _y (pybz) _w	Solution	RT	100	[21]
MFM-300(Al)	Vapor	353	94	[17]
MIL-101(Cr)-TED	Vapor	423	71 ^b	[15]
MIL-101(Cr)-HMTA	Vapor	423	62 ^b	[15]
[(Me ₂ NH) ₂] _x ·[Cd(5-tbip) ₂] _y	Vapor	RT	62	[22]
UiO-66	Solution	RT	40	[19]
MIL-101(Cr)	Vapor	423	13 ^b	[15]

^a RT: room temperature, ^b CH₃I uptake.

S13. H₂S adsorption experiments

Dynamic breakthrough experiments were carried out in a home-made system (Scheme S1). The adsorption column was made from quartz glass with an internal diameter of 7 mm, with a porous glass bed to hold the sample. The adsorption column was covered with a temperature-controlled heating jacket. The column downstream was monitored with a gas chromatograph (HP-5890) equipped with a HP-PLOT 1 column and a thermal conductivity detector (TCD). The GC is equipped with an automatic injection valve.

Sample were activated *in situ* at 373 K for 1 hour with a constant flow of dry N₂ and then slowly cooled to 303 K. Then the H₂S concentration was adjusted with a mass flow controller fed with two lines: dry N₂ and H₂S/N₂ 15 %vol (Scheme S1). The breakthrough experiments were carried out at 303 K and the downstream flow was analysed with a GC, the complete breakthrough of H₂S was indicated by the downstream gas concentration reaching the initial feed.



Scheme S1. Representation of breakthrough system. The H₂S/N₂ mixture passed through a mass flow controller (MFC) which feeds the adsorption column, and a gas chromatograph with a thermal conductivity detector (GC TCD) was used to measure the H₂S downstream.

The H₂S adsorption capacity was calculated using Eq. S11.1, where ‘V_{H₂S}’ represents the H₂S volumetric capacity (cm³ g⁻¹), ‘m’ the adsorbent mass (g), ‘F’ the input flow rate (cm³ min⁻¹), ‘C_f’ and ‘C_t’ the influent and downstream H₂S concentrations respectively (% vol), and ‘t’ the time (min).[23]

$$V_{H_2S} = \frac{F}{c_f \cdot m} \cdot \int_0^t (C_f - C_t) dt \quad \text{Eq. S11.1}$$

As mentioned before, the adsorption column has a porous glass bed thus, a blank run before each experiment was measured to eliminate the adsorption contribution of the column. In Fig. S7 the blue circles represent the adsorption of the column, and the black circles represent the Mg-CUK-1 adsorption. Then the Mg-CUK-1 corrected volumetric capacity ‘V_{H₂S,corr}’ was estimated using Eq. S11.2.

$$V_{H_2S,corr} = V_{H_2S,blank} - V_{H_2S,sample} \quad \text{Eq. S11.2}$$

The H₂S adsorption capacity is often reported as ‘ q_{H_2S} ’ (mol g⁻¹), this value was roughly estimated with the volumetric adsorption capacity ‘ $V_{H_2S,corr}$ ’ (cm³ g⁻¹) and the ideal gas law Eq. S11.3. Where ‘ p ’ is the system pressure (77.3 kPa), ‘ T ’ the measurement temperature (303 K), and ‘ R ’ the ideal gas constant (8314.4598 cm³ kPa K⁻¹ mol⁻¹).

$$q_{H_2S} = \frac{V_{H_2S,corr} \cdot p}{R \cdot T} \quad \text{Eq. S11.3}$$

The breakthrough system was tested with other reported MOF materials (Fig. S16): MOF74(Zn) and HKUST-1.[24] 50 mg of each sample were activated in situ at 453 K for 1 hour with a constant flow of dry N₂ and then slowly cooled to 303 K. Then the H₂S desired concentration was adjusted 6 %vol. Adsorption capacity at 6 %vol of H₂S concentration for the reported materials are correspondent with the reported values (Table S6).

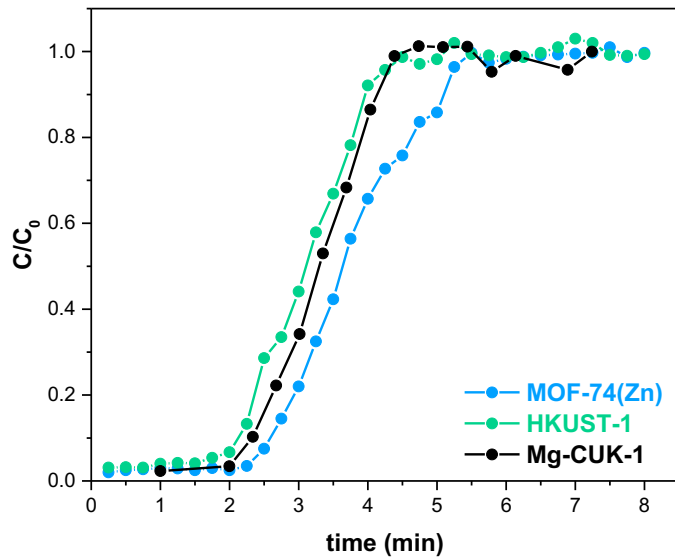


Fig. S20. H₂S adsorption breakthrough curves at 303 K for MOF-74(Zn) and HKUST-1. Measurements using 6 %vol. H₂S/N₂ feed concentration and a 30 cm³ min⁻¹ flow rate.

Table S8. H₂S adsorption capacity for some related MOFs. Breakthrough measurements using 6 %vol. H₂S/N₂ feed concentration and a 30 cm³ min⁻¹ flow rate.

Material	H ₂ S uptake (mmol g ⁻¹)	
	Our System[25]	Reported[24]
Mg-CUK-1	1.41	-
MOF-74(Zn)	1.72	1.64
HKUST-1	1.04	1.1

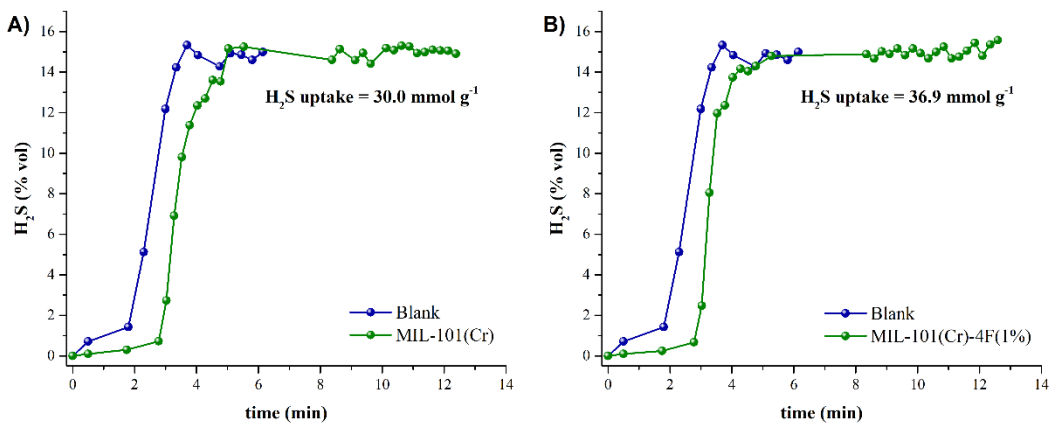


Fig. S21. H₂S adsorption breakthrough curves of A) MIL-101(Cr) and B) MIL-101(Cr)-4F(1%) at 303 K using a 15 %vol. H₂S/N₂ feed concentration. The circles represent the experimental data for the sample (green) and the empty cell (blue). Flow rate was adjusted to 30 cm³ min⁻¹.

Table S9. H₂S adsorption capacity for MIL-101(Cr) and MIL-101(Cr)-4F(1%).

Material	Weight (mg)	V _{H2S} adsorbed (mL)	n _{H2S} adsorbed (mmol)	H ₂ S uptake (mmol g ⁻¹)
MIL-101(Cr)	40.4	30.84	1.24	30.0
MIL-101(Cr)-4F(1%)	35.6	32.76	1.31	36.9

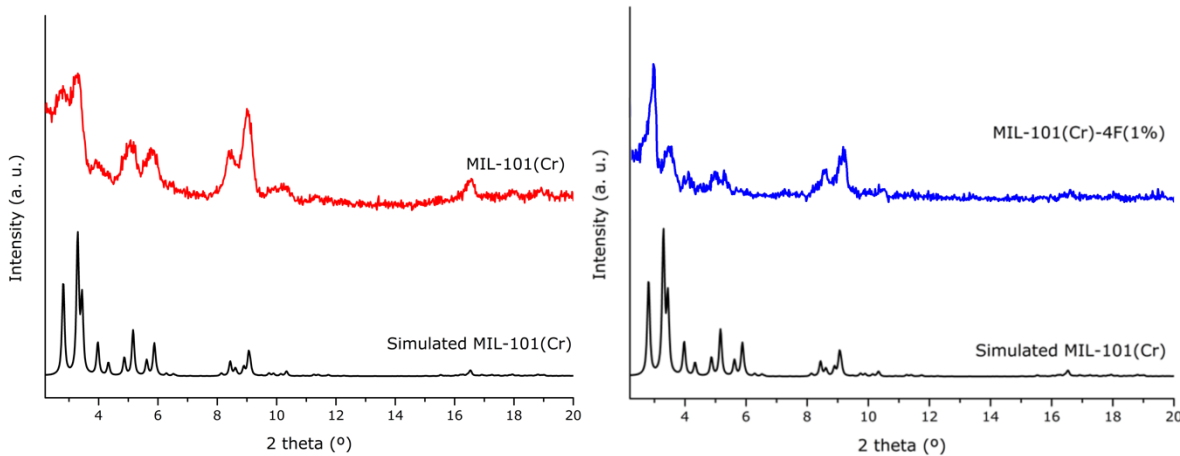


Fig. S22. PXRD of materials after H₂S capture. (left) simulated and MIL-101(Cr) (black), MIL-101(Cr) (red); and (right) simulated MIL-101(Cr) (black) and MIL-101(Cr)-4F(1%) (blue).

References

1. C. F. Macrae, I. J. Bruno, J. A. Chisholm, P. R. Edgington, P. McCabe, E. Pidcock, L. Rodriguez-Monge, R. Taylor, J. van de Streek and P. A. Wood, *J. Appl. Cryst.*, 2008, **41**, 466.
2. Z. Zhao, Z. Li and Y.S. Lin, *Ind. Eng. Chem. Res.*, 2009, **48**, 10015.
3. K. Sumida, D.L. Rogow, J.A. Mason, T.M. McDonald, E.D. Bloch, Z.R. Herm, T.-H. Bae and J.R. Long, *Chem. Rev.*, 2012, **112**, 724.
4. J. B. DeCoste, M. H. Weston, P. E. Fuller, T. M. Tovar, G. W. Peterson, M. D. LeVan and O. K. Farha, *Angew. Chem. Int. Ed.*, 2014, **53**, 14092.
5. D. Alezi, Y. Belmabkhout, M. Suyetin, P. M. Bhatt, Ł. J. Weseliński, V. Solovyeva, K. Adil, I. Spanopoulos, P. N. Trikalitis, A.-H. Emwas and M. Eddaoudi, *J. Am. Chem. Soc.*, 2015, **137**, 13308.
6. P. Z. Moghadam, T. Islamoglu, S. Goswami, J. Exley, M. Fantham, C. F. Kaminski, R. Q. Snurr, O. K. Farha and D. Fairen-Jimenez, *Nat. Commun.*, 2018, **9**, 1378.
7. C. G. Piscopo, F. Trapani, A. Polyzoidis, M. Schwarzer, A. Pace and S. Loebbecke, *New J. Chem.*, 2016, **40**, 8220.
8. S. M. McIntyre, B. Shan, R. Wang, C. Zhong, J. Liu and B. Mu, *Ind. Eng. Chem. Res.*, 2018, **57**, 9240.z
9. Y. Liao, J. Weber, B. M. Mills, Z. Ren and C. F. J. Faul, *Macromolecules*, 2016, **49**, 6322.
10. R. J. Marshall, S. L. Griffin, C. Wilson and R. S. Forgan, *Chem. Eur. J.*, 2016, **22**, 4870.
11. Z. Yan, Y. Yuan, Y. Tian, D. Zhang and G. Zhu, *Angew. Chem. Int. Ed.*, 2015, **54**, 12733.
12. R.-X. Yao, X. Cui, X.-X. Jia, F.-Q. Zhang and X.-M. Zhang, *Inorg. Chem.*, 2016, **55**, 9270.
13. Y. Chen, H. Sun, R. Yang, T. Wang, C. Pei, Z. Xiang, Z. Zhu, W. Liang, A. Li and W. Deng, *J. Mater. Chem. A*, 2015, **3**, 87.
14. D. F. Sava, K. W. Chapman, M. A. Rodriguez, J. A. Greathouse, P. S. Crozier, H. Zhao, P. J. Chupas and T. M. Nenoff, *Chem. Mater.*, 2013, **25**, 2591.
15. B. Li, X. Dong, H. Wang, D. Ma, K. Tan, S. Jensen, B. J. Deibert, J. Butler, J. Cure, Z. Shi, T. Thonhauser, Y. J. Chabal, Y. Han and J. Li, *Nat. Commun.*, 2017, **8**, 485.
16. G. Brunet, D. A. Safin, M. Z. Aghajii, K. Robeyns, I. Korobkov, T. K. Woo and M. Murugesu, *Chem. Sci.*, 2017, **8**, 3171.
17. X. Zhang, I. da Silva, H. G. W. Godfrey, S. K. Callear, S. A. Sapchenko, Y. Cheng, I. Vitorica-Yrezabal, M. D. Frogley, G. Cinque, C. C. Tang, C. Giacobbe, C. Dejoie, S. Rudic, A. J. Ramirez-Cuesta, M. A. Denecke, S. Yang and M. Schröder, *J. Am. Chem. Soc.*, 2017, **139**, 16289.
18. D. F. Sava, M. A. Rodriguez, K. W. Chapman, P. J. Chupas, J. A. Greathouse, P. S. Crozier and T. M. Nenoff, *J. Am. Chem. Soc.*, 2011, **133**, 12398.
19. Z. Wang, Y. Huang, J. Yang, Y. Li, Q. Zhuang and J. Gu, *Dalton Trans.*, 2017, **46**, 7412.
20. G. Mehlana, G. Ramon and S. A. Bourne, *Microporous Mesoporous Mater.*, 2016, **231**, 21.
21. M.-H. Zeng, Q.-X. Wang, Y.-X. Tan, S. Hu, H.-X. Zhao, L.-S. Long and M. Kurmoo, *J. Am. Chem. Soc.*, 2010, **132**, 2561.
22. A. K. Chaudhari, S. Mukherjee, S. S. Nagarkar, B. Joarder and S. K. Ghosh, *CrystEngComm*, 2013, **15**, 9465.
23. P. Nugent, Y. Belmabkhout, S. D. Burd, A. J. Cairns, R. Luebke, K. Forrest, T. Pham, S. Ma, B. Space, L. Wojtas, M. Eddaoudi and M. J. Zaworotko, *Nature*, 2013, **495**, 80.
24. J. Liu, Y. Wei, P. Li, Y. Zhao and R. Zou, *J. Phys. Chem. C*, 2017, **121**, 13249.
25. E. Sánchez-González, P. G. M. Mileo, M. Sagastuy-Breña, J. Raziel Álvarez, J. E. Reynolds III, A. Villarreal, A. Gutiérrez-Alejandre, J. Ramírez, J. Balmaseda, E. González-Zamora, G. Maurin, S. M. Humphrey and I. A. Ibarra, *J. Mater. Chem. A*, 2018, **6**, 16900.